Available online at www.sciencedirect.com
ScienceDirect
Acta Materialia 58 (2010) 6125–6133
Acta MATERIALIA
www.elsevier.com/locate/actamat

Processing and mechanical properties of porous Fe–26Cr–1Mo for solid oxide fuel cell interconnects

J.A. Scott, D.C. Dunand *

Department of Materials Science and Engineering, Northwestern University, Evanston, IL 60208, USA

Received 3 April 2010; received in revised form 15 July 2010; accepted 17 July 2010
Available online 20 August 2010

Abstract

Porous, ferritic steel was produced by blending, pressing and sintering Fe, Cr, Mo and NaCl powders. During sintering NaCl evaporated to form 40–58% interconnected open porosities, while the metal powders densified and interdiffused to create a nearly dense Fe–26Cr–1Mo matrix (E-Brite, developed for solid oxide fuel cell interconnects). The foam compressive properties at ambient temperature were in good agreement with the Gibson–Ashby scaling laws for stiffness and strength and demonstrate high mechanical energy absorption. The foam compressive creep response at 850 °C under an argon atmosphere followed the same power law stress dependence as the bulk material, suggesting similar deformation mechanisms in each case. Creep data under argon were compared with a variational composite model and a simple unit cell model taking into account thicker nodes connecting slender struts.

Keywords: Ferritic steels; Foams; Fuel cell materials; Creep; Cellular materials

1. Introduction

Due to their high efficiency and fuel flexibility [1], solid oxide fuel cells (SOFCs) are attractive as auxiliary power units (APUs) [2–5]. While SOFCs have traditionally been reserved for stationary power applications, recent reductions in operating temperature (to <850 °C) have enabled the replacement of brittle, conductive ceramic interconnects (e.g. Sr- or Ca-doped $LaCrO_3$) with ductile, metallic alloys, thus making SOFCs more compatible with mobile APU applications [3]. Metallic alloys have typically been employed in two types of SOFC architectures: anode-supported cells and metal-supported cells. In the anode-supported configuration a metallic substrate with channels for gases functions as a current collector and physical barrier between the fuel and oxidant [6]. Compared with the previous generation of SOFCs, which utilized ceramic interconnects, the use of a metallic alloy offers a number of benefits, including increased thermal shock resistance (tolerance to rapid thermal cycling), a wide range of low cost, commercially available compositions and ease of assembly and sealing methodologies [6–8]. The second, metal-supported cell design utilizes metallic interconnects, with pores or channels, to support an anode which can be thinner as it is not supporting, resulting in a lighter and less expensive stack design [4,5,9–12].

Limited research has explored the option of porous metals for use as interconnects in SOFCs. Studies have examined Ni felts [13,14] as well as Fe-based alloys such as a Ti- and Nb-stabilized 17% Cr ferritic stainless steel (European designation 1.4509) [2], 430 stainless steel [3], 454 stainless steel [4] Fe30Cr [15,16], and CroFer22APU (Fe–22Cr–0.5Mn–0.1Ti–0.1La in wt.%, ThyssenKrupp VDM) [17]. Most of these substrates were prepared using powder metallurgy techniques with pre-alloyed powders to create open porosities in the range 30–50% [15–18], so as to allow sufficient gas flow across the electrodes [9]. An alternative porous aluminum iron titanate and Fe–30Cr cermet current collector has also been examined for increased thermal expansion matching with the ceramic components of the stack [5]. Much of the previous work on SOFC intercon-

* Corresponding author. Tel.: +1 8474915370.
E-mail address: dunand@northwestern.edu (D.C. Dunand).

1359-6454/$36.00 © 2010 Acta Materialia Inc. Published by Elsevier Ltd. All rights reserved.
doi:10.1016/j.actamat.2010.07.030

nects has focused on ferritic steels due to their low cost, good oxidation resistance and low thermal expansion mismatch with the ceramic stack components. E-Brite is one such alloy that has been well characterized for dense interconnect substrates [7,19,20] but has not yet been tested as a foam.

Most methods for producing Fe-based metallic foams involve casting (liquid-state) or powder metallurgy (solid-state) routes. Casting methods are limited by the high melting point and low melt viscosity of molten steel, which favor techniques using space holders to create porosity [21]. These methods can be applied in a variety of different ways. In the case of precision steel casting, temporary scaffolds consisting of polyurethane [22] or pelleted casting sand [21] have been used to create open porosities [23]. With powder metallurgy place holders such as carbamide (urea) [24,25] are first mixed with a metal powder. The resulting powder blend is then pressed, the place holder is removed via a thermal or chemical process [26] and the compact is subsequently sintered to remove porosity between powders but not porosity left by the space holder.

Relative to other alloys, the types of preforms and place holders used in Fe-based foaming are not well developed. In the case of Al foams combustible place fillers such as polystyrene resin can be used and are subsequently burned out after the pattern has been cast [27]. More commonly though, a leachable scaffold is used as a place holder. One of the most frequently used types, NaCl, has been used extensively for Al foams [28,29], and since then has been utilized with NiTi [30] and amorphous Pd-based [31] foams. Given its low cost, ease of dissolution in water and relatively high melting point, NaCl is a desirable candidate place holder for Fe foams.

While previous research has investigated the electrochemical performance of metal-supported cell stacks utilizing metallic foams, the mechanical behavior of these supports has not yet been studied. Here we examine the ambient and elevated temperature compressive properties of Fe-based metallic foams prepared by the place holder method with open porosities in the range 40–58%. Room temperature results are compared with the Gibson–Ashby scaling laws, while creep properties are validated by existing models for cellular metals.

2. Experimental methods

We used the E-Brite alloy (Fe–26Cr–1Mo, wt.%), which was developed by Allegheny Ludlum (Pittsburgh, PA) for use in SOFC interconnects [7,19,20] due to its coefficient of thermal expansion match with ceramic SOFC components, oxidation resistance and low material cost. Elemental powders of iron (APS 6–10 μm, 99.5% purity), chromium (APS <10 μm, 99.8% purity) and molybdenum (APS 3–7 μm, 99.95% purity) were acquired from Alfa Aesar (Ward Hill, MA). The powders were tumbled in a polymer bottle turned end over end at 30 r.p.m. for 1 h. NaCl powder (99.0% purity, Alfa Aesar, Ward Hill, MA), sieved to 53–106 μm and dried at ~110 °C for 1 h, was added to the mixed metallic powders in the appropriate volume fractions (i.e., 40%, 50% or 60%) and the blend was again mixed end over end for 1 h. The mixed blend was then uniaxially cold pressed at 350 MPa into a 27.9 mm diameter compact. This die press diameter was used in anticipation of shrinkage due to sintering, to produce foams with a diameter of at least 25.4 mm. The compact was vacuum sintered (~10–6 Torr, heating rate 7 °C min^{-1}) at 1250 °C for 4 h, leading to evaporation of the NaCl place holder as well as densification and interdiffusion of the metallic powders. The post-sintering chemical composition of two samples was measured by ATI Wah Chang (Albany, OR) as ~0.01 wt.% for Na and 0.002 wt.% for Cl. Such minute quantities of Na, if dissolved in the E-Brite lattice, are not anticipated to significantly affect the alloy conductivity or the mechanical properties examined in this study. One set of non-porous samples was prepared by melting a 40% porous, post-sintered compact in a vacuum furnace at 1450 °C.

Foams with total porosities within ±5% of the target value were achieved, with a closed porosity of <2% in each case. The closed porosity of each specimen was determined by helium pycnometry with a known bulk E-Brite density of 7.69 g cm^{-3}. To determine the open porosity Archimedes density measurements were performed after coating porous samples with a thin layer of vacuum grease to prevent infiltration of water into the open porosity. When reporting porosity the total (sum of open and closed) porosity is used unless otherwise specified.

Cylindrical compression samples of porous and non-porous specimens were prepared for mechanical testing by wire electro-discharge machining the foams to diameters and heights of either 5 × 10 or 6 × 12 mm. Room temperature compressive behavior was measured with a MTS Sintech 20 G screw-driven load frame containing a 10 kN load cell. Displacement occurred at a rate of 0.05 mm min^{-1} until ~60% strain, or after significant densification of the foam prior to failure. Strain was calculated from crosshead displacement, after correcting for load train compliance.

The creep response of cylindrical as-cast E-Brite samples was measured in compression using an ATS Series 3210 compressive creep frame and ATS Series 2300 tensile creep frame; both systems utilized a constant load, lever arm arrangement. In the case of the tensile frame a superalloy compression cage was used with displacement transmitted by an extensometer attached to a linear voltage displacement transducer (LVDT). Displacement on the compressive frame was also measured by a LVDT, but monitored deflection of the alumina pushrod. In each case displacement was resolved to 6 μm, corresponding to a strain of 0.05%. A testing temperature of 850 °C in laboratory air was chosen to simulate typical SOFC operating conditions and was achieved by means of a three zone, resistively heated furnace with a temperature stability of ±2 °C. However, it was determined that due to the high surface area of

the porous samples, oxide growth was not controllable under these conditions. Foams were therefore tested in the same set-up, but under flowing Ar to reduce most of the oxidation. Overall weight gain under flowing Ar for typical tests of 2–3 days was less than 0.0010 g (or ~0.07%). Constant load creep tests were performed until accumulated engineering strains were 10% in the case of foams or 50% in the case of non-porous samples. Stresses were varied between 0.1 and 12 MPa with up to four increasing applied loads on a single sample. Corresponding secondary creep rates were determined by the slopes of strain–time plots acquired for each sample.

Specimens were mounted in epoxy resin and polished to 0.05 μm using standard metallographic procedures. Optical microscopy and scanning electron microscopy (SEM) were used to examine the microstructures of as-cast E-Brite foams. Samples of non-porous E-Brite were etched by immersion in a glyceregia solution (10 ml HNO_3, 10 ml acetic acid, 15 ml HCl, 2 drops glycerol) for 25 s. A separate electropolishing method was used in the case of porous samples to minimize oxidation of the E-Brite matrix. In this case 1.0 V dc was applied in a 69.4% nitric acid solution for 60 s. Grain size was calculated according to ASTM E112, where the mean lineal intercept was determined by application of a test pattern containing 10 systemically spaced parallel lines of known length.

3. Results

3.1. Microstructure

Representative cross-sections of foams with 43.2%, 52.0% and 58.7% porosity are displayed in Fig. 1. A bimodal distribution of porosity is evident in Fig. 1, with the majority of pores falling in the range ~25–200 μm corresponding to the size range of the NaCl place holders. These pores confirm uniform powder mixing as evidenced by their regular dispersion in the metal. They retain the angular shape of the crushed NaCl powder, which may have a negative effect on some mechanical properties but concurrently leads to an increase in surface area. A second population of closed pores, <10 μm in size and <2% in volume fraction (as determined by helium pycnometry), is also visible, and are due to incomplete sintering of the metallic powders. Grain sizes determined for each of the foam samples in Fig. 1 ranged from 18 to 22 μm, while dense E-Brite was 30 μm.

3.2. Room temperature mechanical properties

Room temperature compressive stress–strain curves for foams of 41.8%, 49.7–50.6% and 57.8–58.1% porosity are shown in Fig. 2 and exhibit behavior typical of ductile metallic foams: a region of linear elasticity followed by a long collapse plateau and, finally, a sharp increase in stress initiating at a strain of ~40% and leading to densification. It is apparent in Fig. 2 that increasing relative density corresponds to an increase in the plastic collapse stress, or yield, of the foam.

Similar to most metallic foams under compressive loading [26,32], a significant amount of energy is absorbed by plastic collapse of the pores, primarily in the plateau region. The magnitude of this stress plateau is strongly dependent upon the yield strength of the bulk material, which helps dictate the resistance of the foam to bending and buckling of struts. A plot of the total accumulated absorbed energy up to strains of 20%, 30% and 50% is given in Fig. 3 for E-Brite foams and is compared with results for a Fe–2.5C foam with porosites in the range 44–57% [33]. The absorbed energy of E-Brite was larger than that for Fe–2.5C, indicating that the lower E-Brite yield strength of ~200 MPa was more than compensated for by its higher ductility.

3.3. Creep properties

A typical strain–time plot is shown in Fig. 4 for a 41.9% porous E-Brite foam tested at 850 °C under a stress of 5.5 MPa. All creep curves exhibited similar behavior, consisting of an initial stage of primary creep followed by a secondary stage where the average strain rate $\dot{\varepsilon}$ was constant. This strain rate is expected to follow a power law behavior:

$$\dot{\varepsilon} = A\sigma_n \exp\left(\frac{-Q}{RT}\right) \quad (1)$$

where σ is the uniaxial applied stress, A is the Dorn constant, n is the stress exponent, Q is the activation energy, R is the gas constant and T is temperature. For simplicity, the Dorn constant and Arrhenius term are commonly combined such that $K = A\exp(-Q/RT)$. Fig. 5 is a double logarithmic plot of minimum strain rate vs. applied stress at a typical SOFC operating temperature of 850 °C for porous and non-porous E-Brite deformed under argon. Porous samples were plotted for three ranges of total porosity

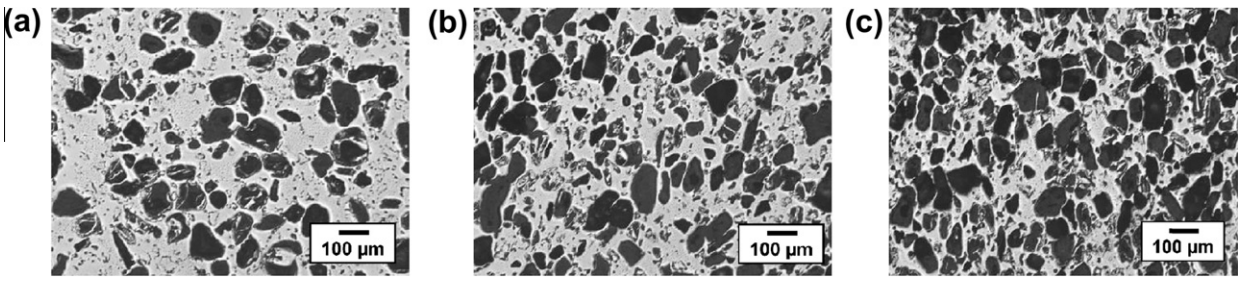

Fig. 1. Optical micrographs of polished cross-sections of E-Brite foams with (a) 43.2%, (b) 52.0% and (c) 58.7% porosity.

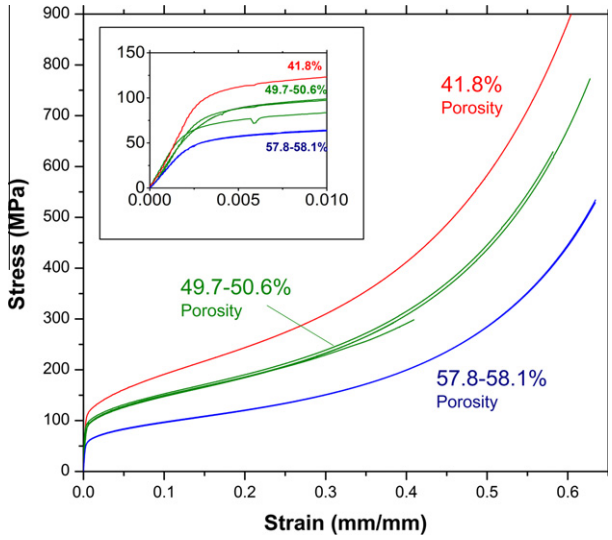

Fig. 2. Room temperature compressive stress–strain curves for 41.8%, 49.7–50.6% and 57.8–58.1% porous E-Brite foams. (Inset) Magnified view of the stress up to 1% strain.

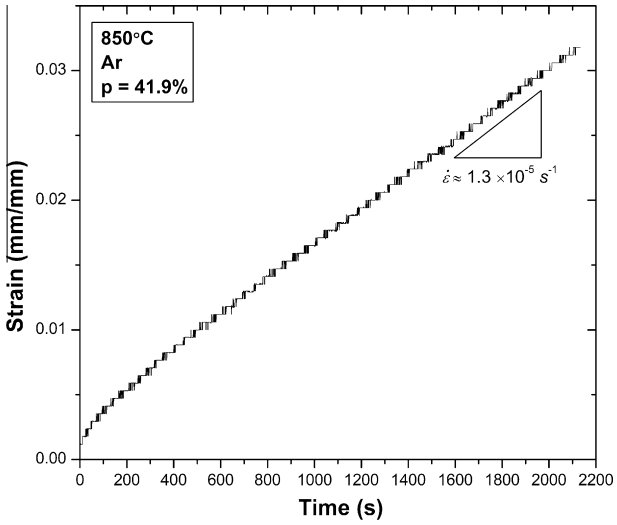

Fig. 4. Typical strain–time plot of an E-Brite foam ($p = 41.9\%$) tested at 850 °C under a stress of 5.5 MPa indicating two regions of behavior, primary creep followed by secondary, steady-state creep.

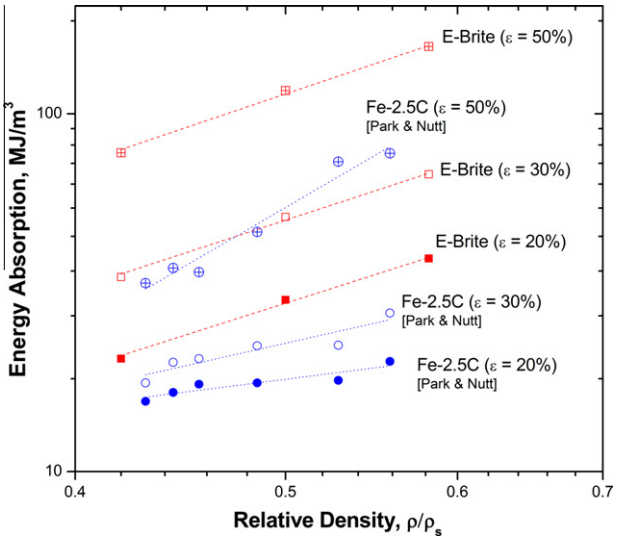

Fig. 3. Energy absorbed per unit volume by E-Brite foams for a range of relative densities ($\rho/\rho_s = 0.42$–0.58) at compressive strains $\varepsilon = 20\%$, 30% and 50%. Data from Park and Nutt [33] for Fe–2.5C foams ($\rho/\rho_s = 0.43$–0.56) are shown for comparison.

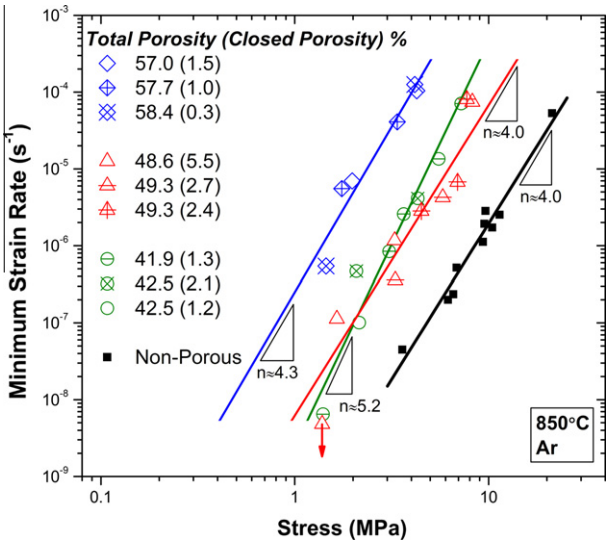

Fig. 5. Compressive minimum creep rate plotted as a function of applied stress for monolithic (non-porous) E-Brite and E-Brite foams with a range of porosities tested at 850 °C under flowing Ar. Closed porosities are listed in parentheses.

(41.9–42.5%, 48.6–49.3% and 57.0–58.4%) that corresponded to best fit apparent stress exponents of 5.2, 4.0 and 4.3, respectively. These match with the data for non-porous samples, which exhibited a best fit value of $n = 4.0$.

Fig. 6 is another creep strain rate vs. applied stress plot for 43.6% and 52.1% porous samples from tests conducted at 850 °C in laboratory air instead of flowing Ar. Significant strengthening is observed (as a steady decrease in strain rate with exposure time, by up to three orders of magnitude) compared with the tests carried out under argon. This strengthening can be assigned to the creation of a strong oxide layer within the foam pores, as illustrated in Fig. 7 showing a polished cross-section of a 52.1% porous foam exposed for 192 h at 850 °C in laboratory air. The scale thickness was ~1 μm (higher values visible in cross-sections may be due to cutting angles close to the scale plane). In some cases the scale appears to choke the open porosity in the foam in these cross-sections (arrows in Fig. 7).

To determine creep activation energy, two samples with a total porosity of $49.4 \pm 0.2\%$ were creep tested at an identical stress of 7.8 MPa under Ar at temperatures of 725 and 750 °C (first sample) and 800 and 850 °C (second sample).

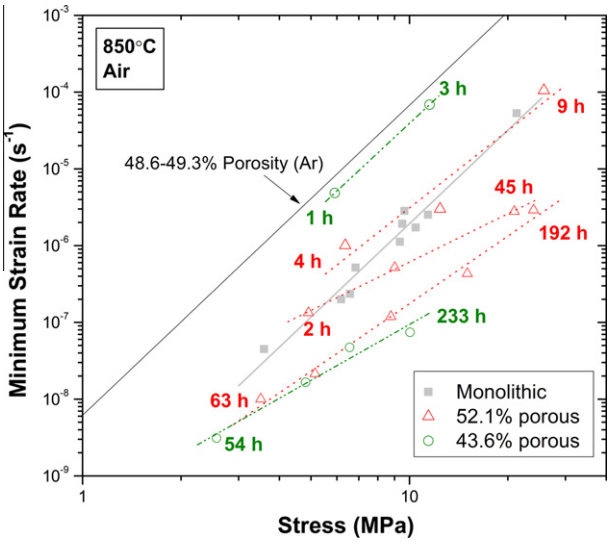

Fig. 6. Compressive minimum creep rate plotted as a function of applied stress for 43.6% and 52.1% porosity E-Brite foams at 850 °C in laboratory air. Total exposure times before and after loading are shown to the left and right of the curves, respectively. A best fit line of data for foams with 48.6–49.3% porosity tested under argon is shown for comparison, along with experimentally determined rates for monolithic E-Brite.

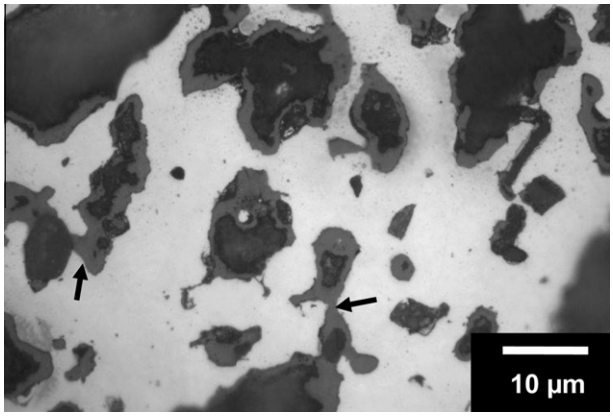

Fig. 7. Optical micrograph of a polished cross-section of a 52.1% porous E-Brite foam after 192 h exposure at 850 °C in laboratory air under no stress. A continuous oxide layer coats all pore surfaces, with potential areas of choking denoted by arrows.

The resulting Arrhenius plot shown in Fig. 8 yields an activation energy of $Q = 290$ kJ mol^{-1}, which is within the broad range of previously reported values for E-Brite: $Q = 239$ kJ mol^{-1} (790–1000 °C), $Q = 251$ kJ mol^{-1} (400–750 °C) [34] and $Q = 316$ kJ mol^{-1} (700–1000 °C) [35].

4. Discussion

4.1. Room temperature mechanical properties

Room temperature compressive properties can be compared with the Gibson–Ashby models for a foam Young's modulus E_f:

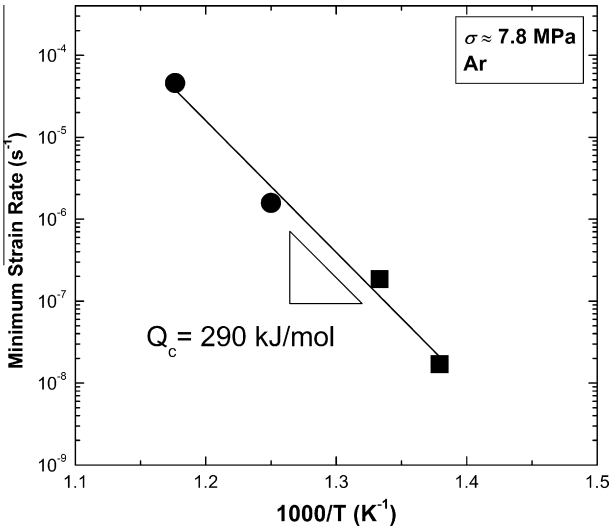

Fig. 8. Compressive minimum strain rate of 49.4% porous E-Brite shown as a function of the inverse of temperature at a constant stress of 7.8 MPa under argon, resulting in an activation energy $Q = 290$ kJ mol^{-1}.

$$E_f = C_E E_s \left(\frac{\rho^*}{\rho_s}\right)^2 \tag{2}$$

and foam yield strength σ_f:

$$\sigma_f = C_\sigma \sigma_s \left(\frac{\rho^*}{\rho_s}\right)^{3/2} \tag{3}$$

where σ_s and E_s are the yield strength and Young's modulus of the bulk material, ρ^*/ρ_s is the relative density of the foam and C is a scaling factor.

Young's modulus was computed from reloading curves after unloading prior to visible plastic deformation, to avoid errors due to initial settling of the sample. Fig. 9

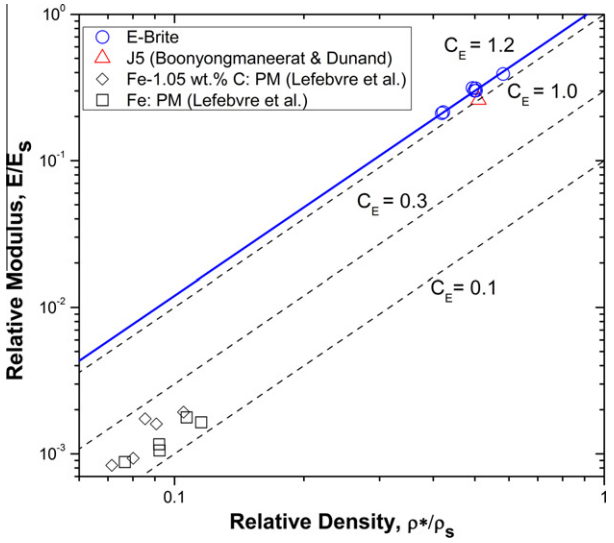

Fig. 9. Dependence of the foam Young's modulus (normalized to the Young's modulus of the solid) upon relative density. Values for various other Fe-based foams of higher porosity are shown, as well as data for a Ni-based SOFC interconnect alloy. Dashed lines indicate common scaling factors of foams according to Eq. (2).

shows experimental data in a plot of the Young's modulus (normalized to the solid Young's modulus) vs. relative density and predictions of Eq. (2), using a solid modulus E_s of 200 GPa for E-Brite [19], for which the value of $C_E = 1.2$ is found. Also plotted in Fig. 9 are values for other Fe-based foams prepared by powder metallurgy [36], as well as a foam made from the Ni-based alloy J5 [37]. The Ni-based foams were created by a similar replication method as the present E-Brite foams; they show the same angular pore shape and therefore display approximately the same value for C_E. Despite similar processing methods, the Fe-based foams with low relative density, yielded values of $C_E \approx 0.1$–0.3. This is indicative of a comparatively lower resistance to elastic deflection. In particular, they lacked the additional mass at the nodes present in the E-Brite and Ni-based alloys that helps resist bending.

The foam compressive yield strength was determined as the intercept of tangents taken from the adjacent pre- and post-yield sections of the stress–strain curve. The resulting values are plotted in Fig. 10 as a function of relative density. Again, good agreement was found with the Gibson–Ashby models using $\sigma_s = 345$ MPa for the compressive yield strength of E-Brite [19] in Eq. (3). The resulting pre-factor $C_\sigma = 0.72$ which fitted the experimental data is above the empirical value $C_\sigma = 0.30$ expected for most foams [38]. When compared with other data for Fe-based foams [33,36,39] and the same Ni-based J5 alloy discussed above [37] used in SOFC interconnects the effect of structure and processing on yield strength are clearly visible. The Fe-based foams at low relative density ($\rho^*/\rho_s < 0.13$) [36] exhibited low C_σ values, as was also observed for stiffness, possibly reflecting flaws or incomplete sintering, as expected from the low sintering temperature. The slip cast Fe-based foams ($\rho^*/\rho_s = 0.42$–0.60) [39], however, were comparatively much stronger, confirming the effect of processing. As the relative density increases above $\rho^*/\rho_s = 0.30$ the beam bending concept used to derive the Gibson–Ashby models becomes invalid [38]. Axial compression dominates over bending and the similar architectures of each of the high relative density foams [37,39] leads to the clustering of high C_σ values in Fig. 10.

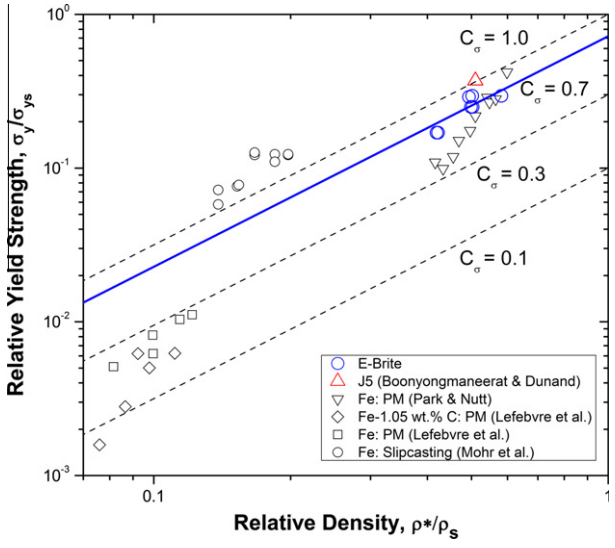

Fig. 10. Dependence of yield strength (normalized to the solid yield strength) upon relative density. Data for other Fe-based foams over a range of porosities is shown in addition to data for a Ni-based SOFC interconnect alloy. Also plotted are dashed lines indicating common scaling factors of foams according to Eq. (3).

4.2. Creep properties

The estimated dependence of creep on relative density was determined by calculating four minimum strain rates corresponding to relative densities in the range 0.42–0.58, which were tested at an identical stress of 1.6 ± 0.1 MPa under argon. Based on the available data plotted in Fig. 11, a best fit power law provides an exponent of 16.2 ± 4.6.

Previous studies on the creep properties of metallic foams have concentrated largely on aluminum and nickel-based reticulated foams with relative densities of 0.15 and below [38,40–43]. Particularly in the case of open cell Al foams [40], creep rates were well predicted by the Gibson–Ashby model for uniaxial creep [38]. In this model deformation is dominated by the creep bending of struts oriented perpendicular to the applied stress while the remaining struts are assumed to be rigid, an assumption which is correct only at low relative densities. An alternative unit cell, valid for higher relative densities, was proposed by [41] and subsequently modified by Hodge and Dunand (HD) [44], in which the struts deform solely in compression along the axis of the applied stress, giving a foam strain rate:

$$\dot{\varepsilon}_f = \left(\frac{V_c}{V_t}\cdot\frac{\rho^*}{\rho_s}\right)^{-n} K\sigma n \tag{4}$$

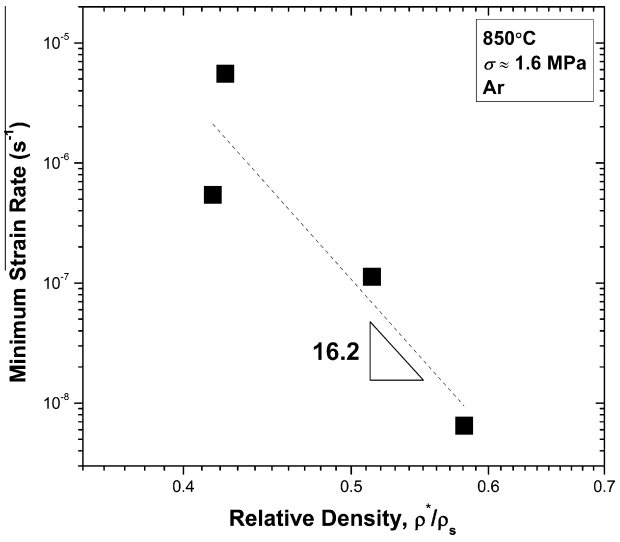

Fig. 11. Plot of minimum compressive strain rate as a function of relative density for a constant temperature of 850 °C and stress of 1.6 MPa under argon.

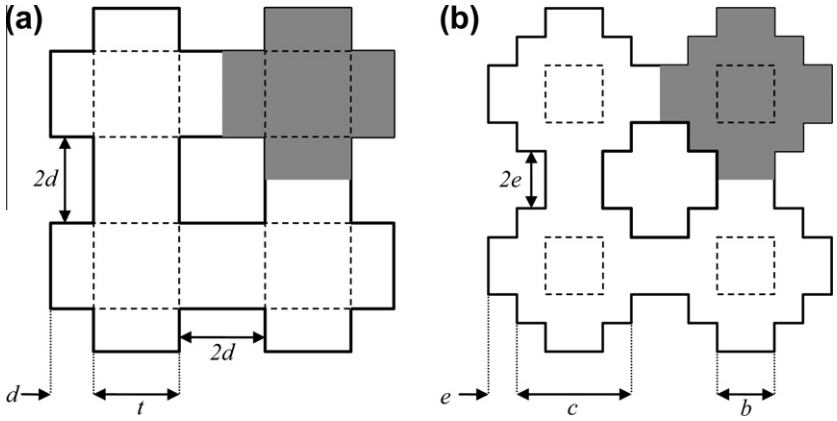

Fig. 12. Structures used to calculate the geometric parameters in the case of: (a) the modified HD model and (b) the concentrated mass HD model.

where V_c/V_t is the ratio of node to strut volume under compressive load over the total volume of nodes and struts and is given by:

$$\frac{V_c}{V_t} = \frac{2dt^2 + t^3}{6dt^2 + t^3} \tag{5}$$

with the geometric parameters d and t defined in Fig. 12a. The resulting strain rate for a 50% porous E-Brite foam calculated according to Eqs. (4) and (5) is superimposed in Fig. 13, alongside experimental data.

As illustrated in Fig. 1, the struts do not have a constant cross-section. A simplified model considers nodes with larger cross-sections than struts. The concentrated mass at the nodes is taken into account via the ratio of vertical struts and nodes under compression to the total volume of the solid in the unit cell [41]:

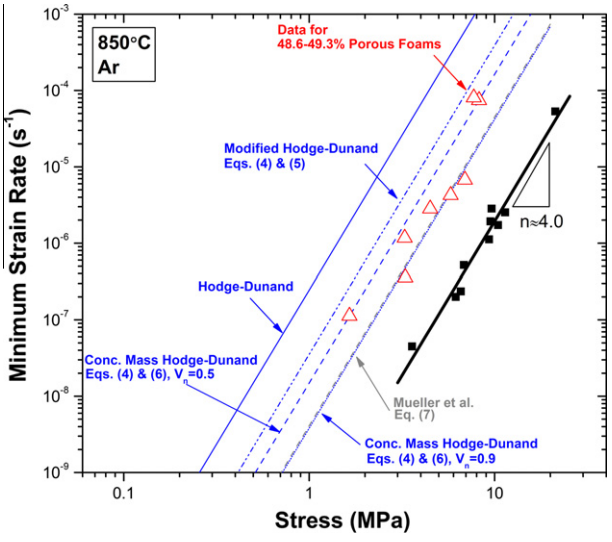

Fig. 13. Theoretical minimum compressive strain rates for 50% porous E-Brite foams predicted by the HD model, the modified HD model (Eqs. (4) and (5)), the concentrated mass HD model (Eqs. (4) and (6)), and the variational model proposed by Mueller et al. [46] (Eq. (7)). Data for 48.6–49.3% porous and monolithic E-Brite are also given.

$$\frac{V_c}{V_t} = \frac{2eb^2 + c^3}{6eb^2 + c^3} \tag{6}$$

with corresponding volumes being defined by the geometric parameters e, b and c as defined in Fig. 12b. In this case the volume concentration at the node V_n (i.e., the volume of material c^3 in the unit cell attributed to the node) can be adjusted as described in the appendix in Boonyongmaneerat [45]. Using V_n values of 0.5 and 0.9, the creep rates of 50% porous E-Brite foam from Eqs. (5) and (6) are plotted in Fig. 13 and nearly bracket the experimental data. The above range of values for this adjustable parameter seems reasonable from the cross-section shown in Fig. 1. Given the distribution of varying nodal to strut volume ratios this model, in particular, provides a useful means of predicting potential creep rates.

Another approach that can be used to predict the strain rate of cellular materials is the variational model adapted by Mueller et al. [46], which yields a simple expression for the steady-state deformation of cellular metals that obey power law creep:

$$\dot{\varepsilon}_f = F_E^{-\left(\frac{1+n}{2}\right)} \left(\frac{\rho^*}{\rho_s}\right)^{-\left(\frac{n-1}{2}\right)} K\sigma n \tag{7}$$

where $F_E = E_F/E_s$. Here, only the K value, stress exponent n, solid modulus E_s and foam modulus E_f need to be known. As a verification of the model, creep data in the form of:

$$\dot{\varepsilon}_{eff} = \dot{\varepsilon}_f = \sqrt{\frac{F_E}{(\rho^*/\rho_s)}} \tag{8}$$

can be plotted as a function of:

$$\sigma_{eff} = \frac{\sigma_f}{\sqrt{F_E(\rho^*/\rho_s)}} \tag{9}$$

where $\dot{\varepsilon}_{eff}$ is the effective strain and σ_{eff} is the effective applied stress. A plot of these values for E-Brite is shown in Fig. 14. Foam data should superimpose directly on top of monolithic values if the foam and bulk material creep undergo the same deformation mechanisms. The scatter

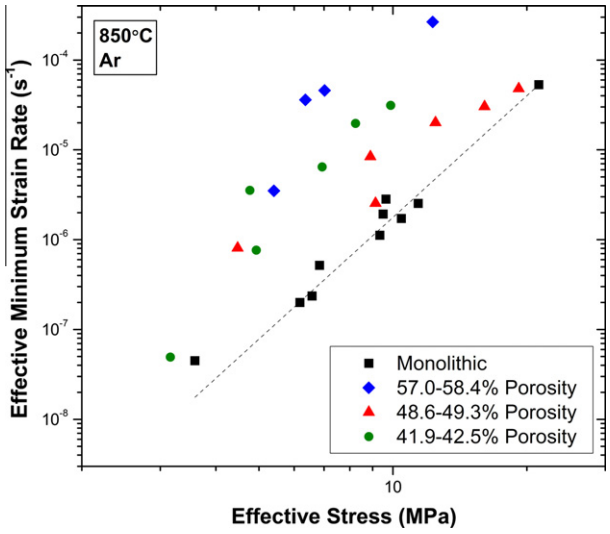

Fig. 14. Plot of effective minimum strain rate (Eq. (8)) in relation to effective applied stress (Eq. (9)) for fully dense and porous E-Brite foams.

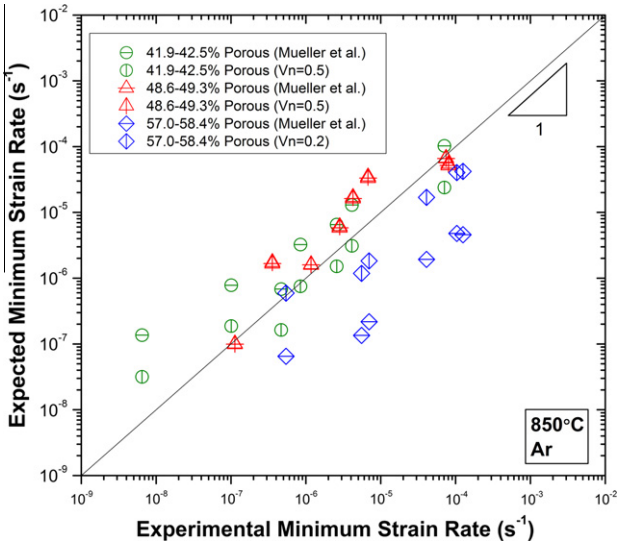

Fig. 15. Plot of calculated vs. experimental minimum compressive creep rates for the E-Brite foams examined in this study. The concentrated mass HD model (Eqs. (4) and (6)) shows good correlation with experimental data, but the volume fraction of the nodes must be adjusted. Variational estimates (without an adjustable parameter) are also plotted (Eq. (7)).

observed in the data, similar to the one to two orders of magnitude variation in strain rate reported by Diologent et al. [47], indicates that the variational model provides a poor estimate of the creep behavior of the present foams. In particular, the predictions worsen with increasing porosity.

A more direct method of comparing the two models consists of plotting experimental vs. predicted values, as in Fig. 15. In the case of the concentrated node HD model (Eq. (6)) nominal porosities of 40%, 50% and 60% were assigned node volumes of 0.5, 0.5 and 0.2, respectively. The variational model was assigned a specific foam modulus based on the Gibson–Ashby scaling law (Eq. (2)) and the pre-factor $C_E = 1.0$. Overall, the concentrated node HD model appears to correlate more closely with the experimental results. However, at ~50% porosity both models estimated almost identical creep behavior. While the variational model provides only a rough approximation of the foam creep behavior without an adjustable parameter, the concentrated node HD model necessitates an adjustable parameter or a measurement (or estimate) of mass concentration at the nodes.

It is important to note that the results of this creep study performed under an Ar atmosphere are most directly applicable to behavior on the cathode side of the SOFC, where the E-Brite would have minimal exposure to an oxidizing environment. In the case of the anode side, the mechanical response of E-Brite must be paired with a better understanding of the oxidation kinetics and reinforcement effects of the oxide layer in order to quantitatively characterize the high temperature response. Nonetheless, as shown in Fig. 6, even short exposure times at 850 °C in an oxidizing environment can lead to a creep resistance superior to that of the dense bulk material.

5. Conclusions

Foams of the ferritic steel E-Brite (an alloy previously developed for SOFC interconnects) with 40–58% porosity were created by a replication powder metallurgy method using NaCl as a temporary place holder. The following conclusions were drawn:

- Foam compressive stiffness and yield strength at room temperature were in good agreement with the Gibson–Ashby scaling laws. Compared with lower density steel foams, E-Brite foams exhibited superior stiffness and strength, which is attributed to mass concentration at the nodes that increases bending resistance. E-Brite also absorbed large amounts of energy in compression due to its high ductility.
- During compressive deformation at 850 °C in air an oxide layer grew within the pores of the foam and became load bearing, thus significantly reducing (by up to two orders of magnitude) the creep rate of the foam.
- For compressive deformation at 850 °C under argon foams exhibited approximately the same stress dependence as dense E-Brite. For a 49% porous foam deformed at 725–850 °C, the creep activation energy was also the same as for dense E-Brite. This indicates that similar deformation mechanisms were at work in the porous and dense materials.
- Creep rates at 850 °C under argon were compared with a variational estimate model and a unit cell model. While the former predicts the strong dependence of the creep rate upon foam density, the latter provides good estimates of creep rate for reasonable values of mass concentration at the nodes of the unit cell.

Acknowledgements

The authors thank Dr. R. Bhat (GE Global Research Center) and Prof. D.J. Lewis (Rensselaer Polytechnic Institute) for useful discussions. Part of this research was funded by NASA through a subcontract from GE (award NNC06CB31C). J.A.S. also thanks Bell Laboratories, the National Science Foundation and the Northwestern University Nanoscale Science and Engineering Center for graduate research fellowships.

References

[1] Steele BC, Heinzel A. Nature 2001;414:345.
[2] Brandon N, Corcoran D, Cummins D, Duckett A, El-Khoury K, Haigh D, et al. J Mater Eng Perform 2004;13:253.
[3] Molin S, Kusz B, Gazda M, Jasinski P. J Power Sources 2008;181:31.
[4] Carter JD, Cruse TA, Bae J, Ralph JM, Myers Deborah J, Kumar R, et al. Mater Res Soc Symp Proc 2003:756.
[5] Matus YB, De Jonghe LC, Jacobson CP, Visco SJ. Solid State Ionics 2005;176:443.
[6] Zhu WZ, Deevi SC. Mater Sci Eng A 2003;348:227.
[7] Fergus JW. Mater Sci Eng A 2005;397:271.
[8] Quadakkers W, Piron-Abellan J, Shemet V, Singheiser L. Mater High Temp 2003;20:115.
[9] Panteix P, Baco-Carles V, Tailhades P, Rieu M, Lenormand P, Ansart F, et al. Solid State Sci 2009;11:444.
[10] Wang Z, Berghaus JO, Yick S, Decès-Petit C, Qu W, Hui R, et al. J Power Sources 2008;176:90.
[11] Tucker MC, Lau GY, Jacobson CP, DeJonghe LC, Visco SJ. J Power Sources 2007;171:477.
[12] Tucker M, Sholklapper T, Lau G, DeJonghe L, Visco S. Progress in metal-supported SOFCs. In: Singhal SC, Yokokawa H, editors. The electrochemical society proceedings, vol. 25. Pennington (NJ): Electrochemical Society; 2009. p. 673.
[13] Lang M, Franco T, Schiller G, Wagner N. J Appl Electrochem 2002;32:871.
[14] Takenoiri S, Kadokawa N, Koseki K. J Therm Spray Technol 2000;9:360.
[15] Villarreal I, Jacobson C, Leming A, Matus Y, Visco S, De Jonghe L. Electrochem Solid State 2003;6:A178.
[16] Antepara I, Villarreal I, Rodriguez-Martinez L, Lecanda N, Castro U, Laresgoiti A. J Power Sources 2005;151:103.
[17] Vaßen R, Hathiramani D, Mertens J, Haanappel V, Vinke I. Surf Coat Technol 2007;202:499.
[18] Arahuetes E, Bautista A, Velasco F, Sotomayor M. Rev Metal 2008;44:406.
[19] ATI Properties Inc. E-Brite alloy for solid oxide fuel cells (UNS designation UNS 44627) technical data. Brackenridge (PA): ATI Allegheny Ludlum; 2002.
[20] Yang Z, Weil KS, Paxton DM, Stevenson JW. J Electrochem Soc 2003;150:A1188.
[21] Pekala RW, Hopper RW. J Mater Sci 1987;22:1840.
[22] Hintz C, Wagner I, Sahm PR, Stoyanov P. Investment cast near net shape components based on cellular metal materials. In: Banhart J, Ashby MF, Fleck NA, editors. Metal foams and porous metal structures. Bremen: MIT Verlag; 1999. p. 153.
[23] Quadbeck P, Kaschta J, Singer R. Adv Eng Mater 2004;6:635.
[24] Bram M, Stiller C, Buchkremer HP, Stover D, Baur H. Adv Eng Mater 2000;2:196.
[25] Bakan HI. Scripta Mater 2006;55:203.
[26] Degischer H, Kriszt B, editors. Handbook of cellular metals: production, processing, applications. Weinheim: Wiley-VCH; 2002.
[27] Ma L, Song Z, He D. Scripta Mater 1999;41:785.
[28] Polonsky L, Lipson S, Markus H. Modern Cast 1961;39:57.
[29] San Marchi C, Mortensen A. Acta Mater 2001;49:3959.
[30] Bansiddhi A, Dunand D. Acta Biomater 2008;4:1996.
[31] Wada T, Inoue A. Mater Trans 2003;44:2228.
[32] Ashby MF, Evans T, Fleck NA, Gibson LJ, Hutchinson JW, Wadley HNG. Metal foams: a design guide. Boston (MA): Butterworth-Heinemann; 2000.
[33] Park C, Nutt SR. Mater Sci Eng A 2000;288:111.
[34] Schmidt C, Young C, Walser B, Klundt R, Sherby O. Metall Mater Trans A 1982;13:447.
[35] Daehn G, Kum D, Sherby O. Metall Mater Trans A 1986;17:2295.
[36] Lefebvre L, Gauthier M, Patry M. Int J Powder Metall 2006;42:49.
[37] Boonyongmaneerat Y, Dunand D. Adv Eng Mater 2008;10:379.
[38] Gibson LJ, Ashby MF. Cellular solids: structure and properties. Cambridge: Cambridge University Press; 1997.
[39] Mohr U, Bleck W, Scholz P. Adv Eng Mater 2002:4.
[40] Andrews EW, Gibson LJ, Ashby MF. Acta Mater 1999;47:2853.
[41] Hodge A, Dunand D. Metall Mater Trans A 2003;34:2353.
[42] Choe H, Dunand DC. Mater Sci Eng A 2004;384:184.
[43] Andrews EW, J- Huang, Gibson LJ. Acta Mater 1999;47:2927.
[44] Boonyongmaneerat Y, Dunand DC. Acta Mater 2009;57:1373.
[45] Boonyongmaneerat Y. Mater Sci Eng A 2007;452–453:773.
[46] Mueller R, Soubielle S, Goodall R, Diologent F, Mortensen A. Scripta Mater 2007;57:33.
[47] Diologent F, Goodall R, Mortensen A. Acta Mater 2009;57:830.